





## Visualization of edge-modulated charge-density-wave orders in monolayer transition-metal-dichalcogenide metal

Quanzhen Zhang<sup>1,7</sup>, Jiahao Fan<sup>2,7</sup>, Teng Zhang <sup>1,7</sup>, Jizhang Wang<sup>2,3</sup>, Xiaoyu Hao<sup>1</sup>, Ying-Ming Xie<sup>4</sup>, Zeping Huang<sup>1</sup>, Yaoyao Chen<sup>1</sup>, Meng Liu<sup>1</sup>, Liangguang Jia<sup>1</sup>, Huixia Yang<sup>1</sup>, Liwei Liu<sup>1</sup>, Huaqing Huang<sup>2</sup>✉, Yu Zhang <sup>1,5</sup>✉, Wenhui Duan <sup>3,6</sup> & Yeliang Wang <sup>1,5</sup>✉

In two-dimensional materials with the many-body quantum states, edges become especially significant for realizing a host of physical phenomena and for potential applications in nanodevices. Here, we report the successful construction of ultra-flat monolayer 1H-phase niobium diselenide (NbSe<sub>2</sub>) with atomically sharp zigzag edges. Our scanning tunneling microscopy and spectroscopy measurements reveal that such zigzag edges hold intriguing one-dimensional edge states. Moreover, we observe an obvious energy-dependent charge-density-wave (CDW) modulation near the edge, highlighting the significant edge-CDW interference interactions. Our findings provide a comprehensive study of tunable structural and electronic properties at the edges in monolayer NbSe<sub>2</sub>. More importantly, the edge-CDW interference model can be feasible for other CDW metals, suggesting a promising direction of extending desired edge functionalities.

<sup>1</sup>School of Integrated Circuits and Electronics, MIIT Key Laboratory for Low-Dimensional Quantum Structure and Devices, Beijing Institute of Technology, Beijing 100081, China. <sup>2</sup>School of Physics, Peking University, Beijing 100871, China. <sup>3</sup>State Key Laboratory of Low Dimensional Quantum Physics and Department of Physics, Tsinghua University, Beijing 100084, China. <sup>4</sup>Department of Physics, Hong Kong University of Science and Technology, Clear Water Bay, Hong Kong, China. <sup>5</sup>Advanced Research Institute of Multidisciplinary Sciences, Beijing Institute of Technology, Beijing 100081, China. <sup>6</sup>Frontier Science Center for Quantum Information, Beijing 100084, China. <sup>7</sup>These authors contributed equally: Quanzhen Zhang, Jiahao Fan, Teng Zhang. ✉email: [huaqing.huang@pku.edu.cn](mailto:huaqing.huang@pku.edu.cn); [yzhang@bit.edu.cn](mailto:yzhang@bit.edu.cn); [yeliang.wang@bit.edu.cn](mailto:yeliang.wang@bit.edu.cn)

Edges in two-dimensional (2D) materials, such as graphene and transition metal dichalcogenides (TMDs), have profound influences on their electrical, optical, and chemical properties<sup>1–4</sup>. In contrast to graphene with the well-known zigzag (ZZ) and armchair edges<sup>5,6</sup>, the edges in TMDs are expected to become more abundant and significant. On the one hand, TMDs, consist of the formula  $\text{MX}_2$  where M is a transition metal and X is a chalcogen, possess a diversity of atomic compositions and configurations at the edge<sup>7–9</sup>. On the other hand, TMDs hold potentials of various many-body quantum states including charge/spin density waves and superconductivity<sup>10–14</sup>, the edges of which provide a compelling platform to realize more physical phenomena and unique functionalities.

Although there have been long-standing theoretical and experimental interests and efforts on the edge properties of TMDs, the experiments still suffered from the uncontrollable construction of the specific edge structures. Moreover, the direct spectroscopic identification of the structure-dependent edge states especially at the atomic level, and the microscopic understanding of how the edges influence the many-body quantum states in TMDs, remain significantly challenging.

Niobium diselenide ( $\text{NbSe}_2$ ) with H-phase is a model material for exploring many-body electronic physics, as it hosts charge-density-wave (CDW) order and superconductivity in the monolayer limit<sup>15–17</sup>. In this work, we systematically study the constructed control over the edge structures in monolayer 1H- $\text{NbSe}_2$  (hereinafter simply  $\text{NbSe}_2$ ) at the atomic level and their modulation on the electronic properties. Our scanning tunneling microscopy/spectroscopy (STM/S) measurements, complemented by density functional theory (DFT) calculations, indicate that the

edges in monolayer  $\text{NbSe}_2$  prefer to exhibit ZZ configurations. Moreover, we observe obvious one-dimensional (1D) edge states along the ZZ edges, together with the edge-induced CDW modulation on the interior of monolayer  $\text{NbSe}_2$ . Our results provide a comprehensive study of the edge states and edge-CDW interference interactions in monolayer  $\text{NbSe}_2$ , and such edge-CDW interference model can be extended to other CDW metals.

## Results and Discussions

**Edge states of monolayer  $\text{NbSe}_2$ .** Figure 1a shows a schematic of monolayer  $\text{NbSe}_2$ . A Nb layer is sandwiched by two Se layers, with each Nb atom locating inside a trigonal prismatic cage formed by six nearest-neighbor Se atoms. In our experiments, high-quality monolayer  $\text{NbSe}_2$  islands were prepared on bilayer graphene (BLG)/SiC(0001) substrates by using a molecular beam epitaxy (MBE) method in a Se-rich atmosphere (see methods and Supplementary Fig. 1). Figure 1b shows a large-scale STM topographic image of the as-grown sample surfaces measured at the liquid helium temperature. A close examination of the atomically resolved STM image in Fig. 1c reveals that the topmost Se atoms of  $\text{NbSe}_2$  dominate the topography as bright protrusions<sup>18,19</sup>. Moreover, the commensurate  $3 \times 3$  CDW superlattice aligned with the  $1 \times 1$  atomic lattice for monolayer  $\text{NbSe}_2$  can be clearly identified, which is also evident in the corresponding 2D fast Fourier transform (FFT) image, as shown in Fig. 1d.

Such an ultra-flat monolayer  $\text{NbSe}_2$  island provides us an ideal platform to study the edge properties. Firstly, we concentrate on the structural configurations at the edge. Figure 1e, f show

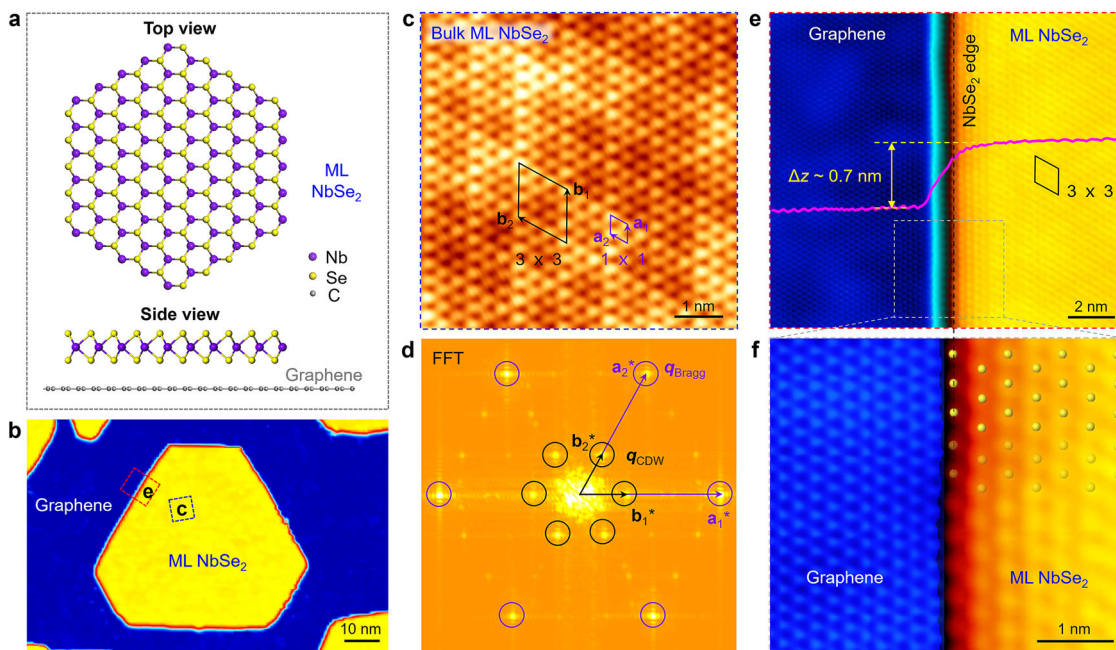


**Fig. 1** Edge structures of monolayer (ML)  $\text{NbSe}_2$ . **a** Side and top views of the atomic structures of ML  $\text{NbSe}_2$  on graphene. Nb, Se, and C atoms are displayed by purple, yellow, and gray spheres, respectively. **b** Large-scale scanning tunneling microscopy (STM) image of a high-quality ML  $\text{NbSe}_2$  island on bilayer graphene (BLG)/SiC(0001) (sample bias:  $-0.1$  V, tunneling current:  $5$  pA). **c** Atomic-resolution STM image of the bulk ML  $\text{NbSe}_2$ , as marked by the dashed blue square in panel b (sample bias:  $-0.1$  V, tunneling current:  $1$  nA). The top Se atoms dominate the STM image, exhibiting a commensurate  $3 \times 3$  charge-density-wave (CDW) superlattice.  $a_1/a_2$  and  $b_1/b_2$  denote the basis vectors of atomic lattice and CDW superlattice, respectively. **d** Fast Fourier transform (FFT) of the topographic STM image shown in panel c. The outer six purple circles indicate the Bragg lattices of  $\text{NbSe}_2$ , and the inner six black circles are related to the CDW orders in  $\text{NbSe}_2$  with  $q_{\text{CDW}} \approx q_{\text{Bragg}}/3$ .  $a_1^*/a_2^*$  and  $b_1^*/b_2^*$  denote the reciprocal basis vectors of atomic lattice and CDW superlattice, respectively. **e** Atomic-resolution STM image at the edge of ML  $\text{NbSe}_2$  island (sample bias:  $-0.1$  V, tunneling current:  $1$  nA). The height profile across the edge shows the apparent height  $\Delta z$  of the island is about  $0.7$  nm, indicating the  $\text{NbSe}_2$  is one-layer thickness. **f** Zoomed-in STM image of the dashed gray rectangle in panel e (sample bias:  $-0.1$  V, tunneling current:  $1$  nA). The atomic structures of the top Se atoms are superposed on the image, demonstrating that the edge of ML  $\text{NbSe}_2$  exhibits a well-ordered zigzag configuration.

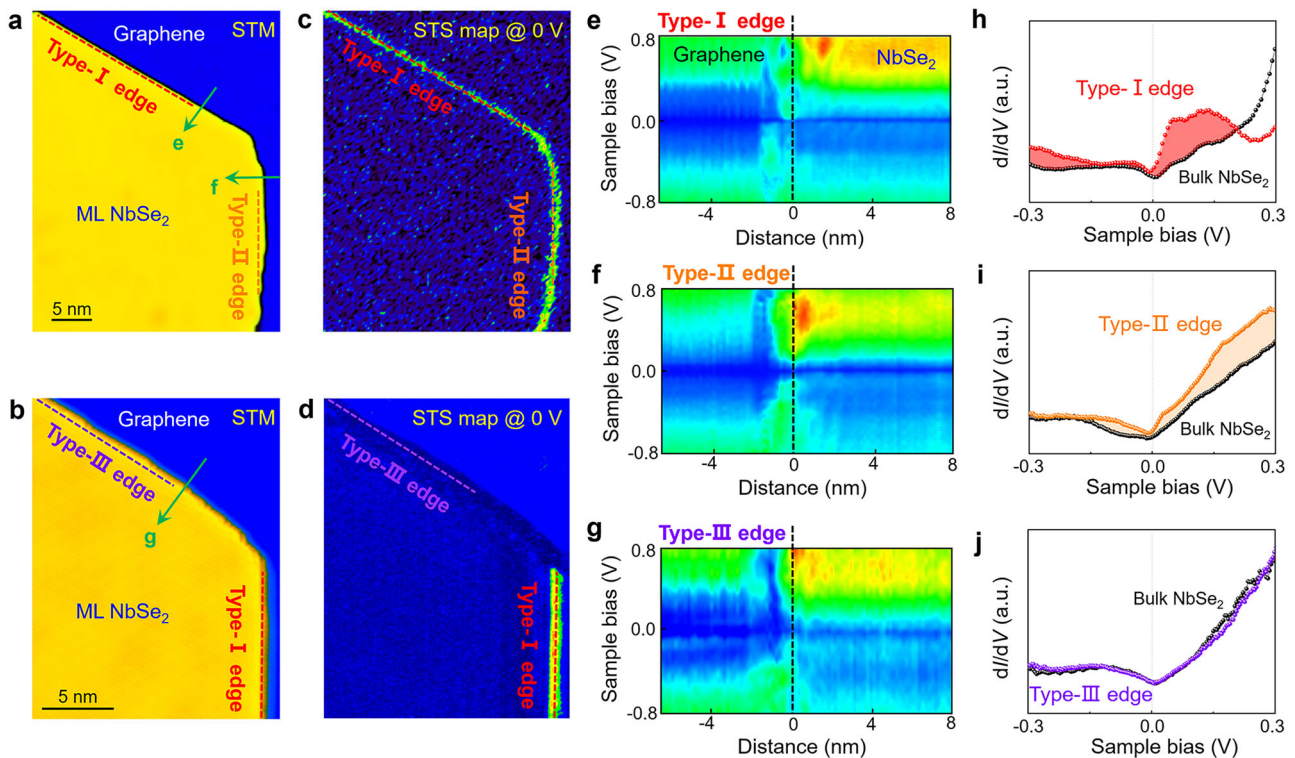


**Fig. 2 Electronic properties at the zigzag (ZZ) edges in monolayer (ML) NbSe<sub>2</sub>.** **a, b** Representative scanning tunneling microscopy (STM) images of ML NbSe<sub>2</sub> islands with ZZ edges. The island edges are marked by the dashed lines. **c, d** Corresponding scanning tunneling spectroscopy (STS) maps recorded at the same locations of panel **a, b** under the energy of 0 eV, respectively. **e–g** Spatially resolved STS spectra recorded across the ZZ edges that marked by the green arrows in panels **a, b**, respectively. The locations of the edges are highlighted by the black dashed lines. **h–j** Low-energy STS spectra at the edges and the bulk of ML NbSe<sub>2</sub> that are extracted from panels **e–g**, respectively. The edge states are highlighted by the shadows.

representative atomic-resolution STM topographic images of an edge in monolayer NbSe<sub>2</sub> island, with an expected apparent height of about 0.7 nm<sup>20,21</sup>. In our cases, the most edges are identified to be a well-ordered ZZ configuration.

Next, we experimentally study the electronic properties at the edge of monolayer NbSe<sub>2</sub> by means of STS measurements. Figure 2a, b shows two typical STM topographic images of monolayer NbSe<sub>2</sub> islands on graphene before and after the thermal annealing process, respectively. All the edges marked by the dashed lines are ZZ, with no obvious distinction in the atomic-resolution STM images (see Supplementary Fig. 2. Note that only the topmost Se atoms of NbSe<sub>2</sub> have contributions to the STM contrast). The spectroscopic measurements, however, highlight significant differences for these edges. For example, the 1D electronic densities along the edges at the Fermi energy ( $E_F = 0$  eV) emerge at both two adjacent edges for the former island (Fig. 2c), while only alternately emerge for the latter one (Fig. 2d).

Having realization of the differences among these ZZ edges in monolayer NbSe<sub>2</sub>, we carry out the spatial-resolved STS measurement for in-depth understanding the connection of the edge states to the bulk. Figure 2e, g show representative STS spectra recorded across the ZZ edges in monolayer NbSe<sub>2</sub> that marked by the arrows in Fig. 2a, b, respectively, and the spectra acquired at the edges and the bulk of NbSe<sub>2</sub> are extracted in Fig. 2h–j and Supplementary Fig. 3. Far from the edge, in the bulk of monolayer NbSe<sub>2</sub>, the STS spectra can be understood on the basis of the monolayer NbSe<sub>2</sub> band structure. There are two pronounced local density-of-state (LDOS) peaks at the energies of about 0.5 eV and  $-0.2$  eV (Fig. 2h), which are attributed to

the conduction band (CB) and valence band (VB), respectively, in accordance with previous studies<sup>17,22,23</sup> and our DFT calculations (Supplementary Fig. 4).

As approaching to the ZZ edges in monolayer NbSe<sub>2</sub>, obvious 1D electronic states appear along the edges, which are confined into a few lattice spacings in the orthogonal direction. Intriguingly, there are three distinct types of edge states with the spatially-resolved STS spectra, as shown in Fig. 2e–g, respectively (corresponding local spectra are shown in Fig. 2h–j). From tens of monolayer NbSe<sub>2</sub> islands, we find that in most cases of the islands with a hexagonal shape in our as-grown samples (Fig. 2a), the STS spectra recorded at the adjacent edges exhibit as Fig. 2e, h (type-I edge) and Fig. 2f, i (type-II edge), respectively. In rare cases, the STS spectra exhibit as Fig. 2g, j (type-III edge). Moreover, the ratio of type-III edges dramatically increases after the thermal annealing process, especially for the cases of the alternate edges in islands with a hexagonal shape (Fig. 2b) and all the edges in islands with a triangular shape (Supplementary Figs. 5–7).

To understand the above experimental phenomena, we carry out DFT calculations of both the charge densities and the electronic band structures at the ZZ edges in monolayer NbSe<sub>2</sub> (more details are given in Supplementary Figs. 8–11 and Supplementary Note 1)<sup>24–26</sup>. As shown in Fig. 3a–c, there are obvious electronic densities for the ZZ-Se (Se edge with Se termination) and ZZ-Nb-Se (Nb edge with Se termination) edges at  $E_F$ . The corresponding band structures in Fig. 3d–f further demonstrate that the localized edge states of the ZZ-Se and ZZ-Nb-Se edges are much stronger than that for ZZ-Nb edge around  $E_F$ , while the edge states of the ZZ-Nb edge are

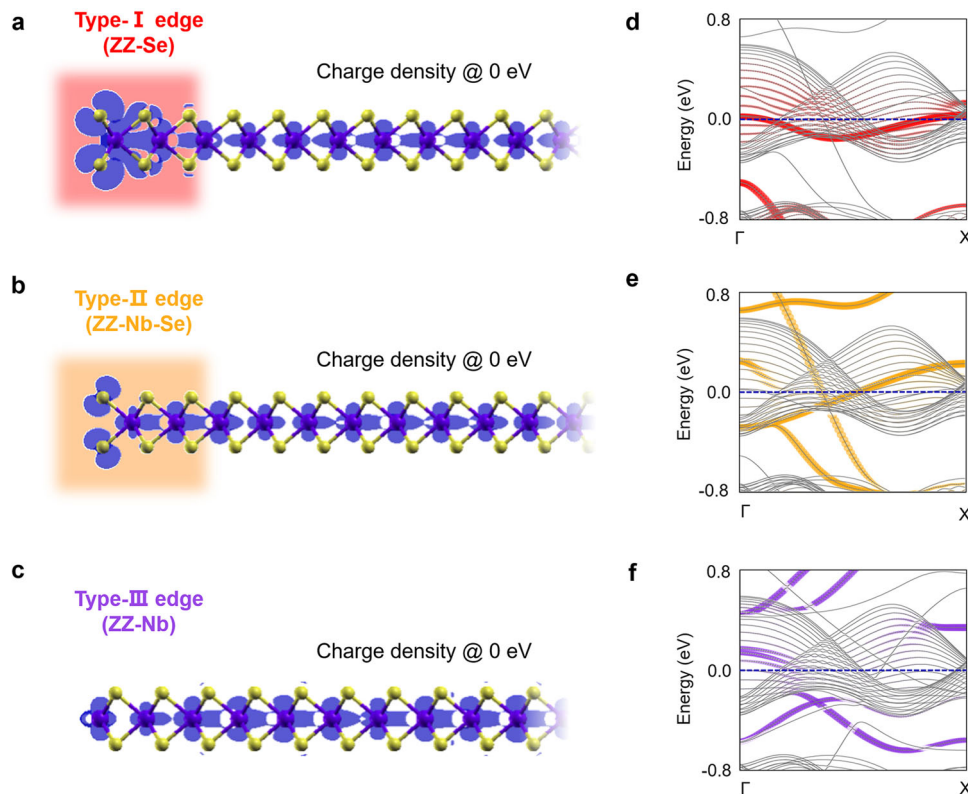


**Fig. 3** Density functional theory (DFT) calculations of both the charge densities and the electronic band structures at the zigzag (ZZ) edges in monolayer NbSe<sub>2</sub>. **a–c** Atomic configurations of the monolayer NbSe<sub>2</sub> ZZ nanoribbons with type-I (ZZ-Se), type-II (ZZ-Nb-Se), and type-III (ZZ-Nb) edges, respectively. The spatially resolved charge densities at Fermi energy ( $E_F$ ) are superposed on the configurations. **d–f** Electronic band structures for the type-I, II, III edges in monolayer NbSe<sub>2</sub>. The edge states are highlighted by the colored dots, and the sizes of the dots represent the proportion of the edge Se/Nb orbitals to the energy bands. The Fermi energy  $E_F$  is marked by the dashed lines.

mainly at  $-0.6$  to  $-0.2$  eV and  $0.5$  to  $0.8$  eV. It's worth noting that such edge states are insensitive to the CDW phase transition<sup>23,27</sup> (Supplementary Table 1, Supplementary Figs. 12 and 13), implying the dominance of the terminated atoms at the ZZ edges in monolayer NbSe<sub>2</sub>.

Now we can identify that the atomic configurations of the types-I, II, III edges shown in Fig. 2 are the ZZ-Se, ZZ-Nb-Se, and ZZ-Nb edges, respectively, with a combination of experimental observations and theoretical calculations (Fig. 3 and Supplementary Figs. 5–7). The configurations of the ZZ edges, which strongly depend on the sample preparation and thermal annealing processes, are supposed to be owing to the edge formation energies<sup>24</sup>. A Se-rich atmosphere ( $\mu_{\text{Se}} \rightarrow 0$ ) can structurally stabilize the Se-terminated ZZ edges with the type-I and II configurations (Supplementary Fig. 14 and Supplementary Note 2). Moreover, the outmost dangling Se atoms prefer to deviate from the bulk monolayer NbSe<sub>2</sub> during the thermal annealing of samples at the temperature of 770 K, thus yielding the Nb-terminated ZZ edge with the type-III configuration. Our results not only demonstrate an avenue to control the monolayer NbSe<sub>2</sub> with specific ZZ edges, but also provide a direct spectroscopic identification of the edge configurations at the atomic level.

In addition, we calculate the electronic band structures of ZZ edges in monolayer NbS<sub>2</sub>, TaS<sub>2</sub>, and TaSe<sub>2</sub>, in order to systematically study the localized edge states in TMD metals with the formula MX<sub>2</sub>. As summarized in Supplementary Fig. 15, the ZZ edge states in all the systems show obvious termination-dependent behaviors, similar to those in monolayer NbSe<sub>2</sub>. For instance, there are usually the charge densities at  $E_F$  for

X-terminated edges, but not for M-terminated edges. Such results indicate a universal phenomenon on the edge states of monolayer TMD metals, paving the way of their functionalization.

**Edge-CDW interactions in monolayer NbSe<sub>2</sub>.** Now we focus on the CDW ground state, one of the most significant many-body quantum states, at the ZZ edges in monolayer NbSe<sub>2</sub> (Fig. 4a, b). Here we take the type-III (ZZ-Nb) edge as an example. Considering that the CDW features are the combination of lattice distortions and charge ordering, we carry out both the STM topography (Fig. 4a) and energy-dependent STS maps (Fig. 4c–e) and Supplementary Fig. 16, in order to provide a clear microscopic understanding of the edge-CDW interference interactions. The atomically resolved STM images on the interior of monolayer NbSe<sub>2</sub> near the well-ordered ZZ edges exhibit clear  $3 \times 3$  superlattices, and the intensities of three CDW vectors  $q_{\text{CDW}} \approx 1/3k_{\text{Bragg}}$ , connected by a three-fold rotation symmetry in the corresponding FFT images, are almost the same (see the region marked by the black rectangle in Fig. 4a), illustrating an atomically sharp edge.

However, the spatial distributions of the charge density in monolayer NbSe<sub>2</sub> show obvious energy-dependent features. Figure 4c–e are the atomically resolved STS maps recorded at the location marked by the black rectangle in Fig. 4a under the energies of  $-0.2$ ,  $0.2$ , and  $0.3$  eV, respectively. In the bulk of defect-free monolayer NbSe<sub>2</sub>, the CDW contrast in the STS maps always exhibits a  $3 \times 3$  CDW order, and the spatial distributions of the charge density in each CDW supercell exhibit an obvious energy-dependent feature (more details are given in Supplementary Fig. 17).

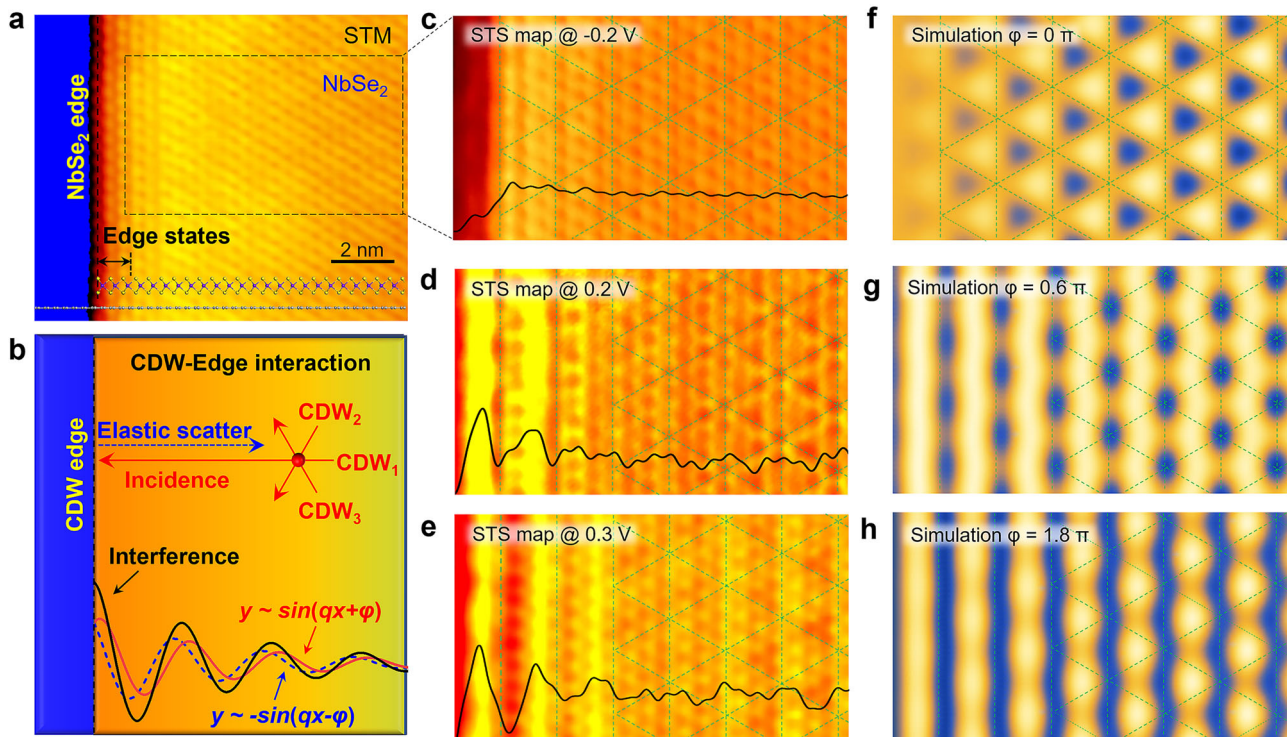


**Fig. 4** Charge-density-wave (CDW) orders on the interior of monolayer (ML) NbSe<sub>2</sub> near the well-ordered zigzag (ZZ) edges. **a** Scanning tunneling microscopy (STM) images at the ZZ edge of ML NbSe<sub>2</sub>. The entire regions exhibit clear 3 × 3 superlattices. The range of edge states are marked in the panel. **b** Schematic diagram of edge states and edge-CDW interference interactions at the CDW edge. The in-plane CDW modulations can be described as the sum of three individual plane waves CDW<sub>1,2,3</sub>, which are connected by a threefold rotation symmetry. In the direction perpendicular to the edge, the incident and elastic scattered waves can be simplified to  $\sin(kx + \varphi)$  and  $-\sin(kx - \varphi)$ , respectively. The interference of the plane waves by the incident and elastic scattered processes results in the stripe-like charge density, depending on the phase  $\varphi$  of the plane wave. **c–e** Atomically resolved scanning tunneling spectroscopy (STS) maps recorded at the location marked by the black rectangle in panel a under the energies of −0.2, 0.2, and 0.3 eV, respectively. In the bulk of defect-free NbSe<sub>2</sub>, the CDW contrast in the STS maps always exhibits a 3 × 3 CDW order, along with the strong charge modulation within each CDW supercell. While on the interior of NbSe<sub>2</sub> near the edges, the CDW contrast changes from 3 × 3 CDW orders to nearly one-dimensional stripe phases. **f–h** Simulations of edge-induced CDW interference with  $\varphi = 0\pi$ ,  $0.6\pi$ , and  $1.8\pi$ , respectively.

On the interior of monolayer NbSe<sub>2</sub> near the well-ordered ZZ edges, however, the spatial distributions of the charge density become quite unique. As changing the sample bias (energy), the charge density varies from the original 3 × 3 CDW order (−0.2 eV, Fig. 4c) to the one-dimensional stripe-like feature (0.2 and 0.3 eV, Fig. 4d, e). It's worth noting that the spacing of the stripes is always a constant, yielding three times of the lattice constant perpendicular to the edge. Such results are repeatable and can also be captured around other types of edges (Supplementary Fig. 18), and show obvious temperature-dependent feature (Supplementary Fig. 19). In our experiments, the distance of edge-CDW interference interactions reaches the maximum of about 3.6 nm when the sample bias is −0.3 V, as shown in Supplementary Fig. 20. Moreover, from the energy-dependent line cut of the STS maps in Fourier space (Supplementary Fig. 21), we can find that the reciprocal vector of the stripes, which always equals to  $1/3k_{\text{Bragg}}$ , strongly rely on the CDW order. As a result, we can rule out the effect of the quasi-particle interference (QPI) and Friedel oscillation near step edges<sup>28–31</sup>.

Such a result, which has never been observed before, can be well understood by the edge-induced CDW interference<sup>32–34</sup>. Theoretically, the in-plane CDW modulations can be described as the sum of three individual plane waves, *i.e.* CDW<sub>1,2,3</sub>, which are connected by a threefold rotation symmetry (Fig. 4b). For each plane wave  $\Psi_n = A_n(\mathbf{r})\sin(\mathbf{q}_n \cdot \mathbf{r} + \varphi_n(\mathbf{r}))$ , there is a specific phase  $\varphi_n$ , depending on the reference point ( $\mathbf{q}_{n=1,2,3}$  are the

momentum vectors of the CDW modulations in three directions,  $A_n$  are the amplitudes of the plane waves). In the absence of any structural defects, the  $\varphi_n$  of three plane waves are arbitrary, yielding a well-ordered CDW modulations of three coexisting components (see STS maps of the bulk monolayer NbSe<sub>2</sub> in Fig. 4c–e).

The atomically sharp ZZ edges in monolayer NbSe<sub>2</sub> are expected to break such a threefold rotation symmetry. At a given STM tip position, the charge modulations are governed by the interference of the CDW plane waves during the incident and elastic scattered processes. In the direction perpendicular to the edge, the momentum vector of the scattered CDW wave changes from  $\mathbf{q}_n$  to  $-\mathbf{q}_n$ , yielding a nonzero phase shift with respect to the incident waves (schematic model is shown in Fig. 4b,  $\varphi$  depends on the recorded energy<sup>33,34</sup>). Therefore, at the specific energies, the interference between the incident and elastic scattered waves are expected to introduce 1D stripes on the interior of monolayer NbSe<sub>2</sub> near the well-ordered ZZ edges, as simulated in Fig. 4f–h and Supplementary Fig. 22 with different  $\varphi$  (more details are given in Supplementary Note 3). More importantly, such edge-CDW interference model can be feasible for other 2D CDW metals, providing potential applications in CDW-based electronic devices such as logic circuits, nonvolatile memory, photodetector, and CDW-based oscillator.

In summary, we provide an in-depth understanding of the structural and electronic properties of the ZZ edges in ultra-flat

monolayer NbSe<sub>2</sub> islands. Combined with the MBE methods, STM/STS measurements, and DFT calculations, we experimentally realize three types of ZZ edges in monolayer NbSe<sub>2</sub>. All the zigzag edges in monolayer NbSe<sub>2</sub> hold intriguing one-dimensional edge states, which are strongly dependent on the terminated atoms. Moreover, there exists an obvious energy-dependent CDW modulation near the edges, varying from an ordinary 3 × 3 CDW order to a nearly stripe phase. Our edge-CDW interference model can be feasible for other 2D CDW metals, suggesting a promising direction of extending desired edge functionalities.

## Methods

**Sample preparation and STM measurements.** The sample preparation and STM measurements were carried out by a custom-designed Unisoku STM system (USM-1300). First, the bilayer graphene (BLG) was obtained by thermal decomposition of 4H-SiC(0001) at 1200 °C for 45 min. And then, the monolayer 2H-NbSe<sub>2</sub> islands were epitaxially grown on bilayer graphene (BLG)/SiC(0001) substrate by evaporating Nb and Se from an electron beam evaporator and a Knudsen cell evaporator, respectively. The flux ratio of Nb and Se is approximately 1:10, in order to guarantee a rich Se environment. The growth rate of NbSe<sub>2</sub> is 0.002 ML/min. The BLG/SiC(0001) substrate was maintained at 500 °C during the growth, followed by a post-annealing process at 200 °C for 20 min.

The STM and STS measurements were performed in the ultrahigh vacuum chamber (~10<sup>-11</sup> Torr) with constant-current scanning mode. The experiments were acquired at the temperature of 4.2 K. An electrochemically etched tungsten tip was used as the STM probe, which was calibrated by using a standard graphene lattice, a Si (111)-(7 × 7) lattice, and an Ag (111) surface. The STS measurements were taken by a standard lock-in technique with the bias modulation of 5 mV at 973 Hz.

**First-principles calculations.** First-principles calculations were performed within the framework of density functional theory (DFT) as implemented in the Quantum Espresso package (QE). A kinetic-energy cutoff of 40 Ry (~544 eV) was used for the plane-wave expansion of the valence wavefunctions, and we adopted a generalized gradient approximation with the Perdew-Burke-Ernzerhof exchange-correlation functional. The edge-state properties are calculated using nanoribbon structures with a width of ~100 Å to reduce the influence of edge states on opposite boundaries. A 11 × 1 × 1 Monkhorst-Pack mesh grid for the Brillouin zone sampling is employed in the self-consistent calculation.

## Data availability

All data needed to evaluate the conclusions in the paper are present in the paper and/or the Supplementary Materials. Additional data related to this paper are available from the corresponding author upon reasonable request.

Received: 27 December 2021; Accepted: 26 April 2022;

Published online: 12 May 2022

## References

- Wang, Q. H., Kalantar-Zadeh, K., Kis, A., Coleman, J. N. & Strano, M. S. Electronics and optoelectronics of two-dimensional transition metal dichalcogenides. *Nat. Nanotech.* **7**, 699–712 (2012).
- Chhowalla, M. et al. The chemistry of two-dimensional layered transition metal dichalcogenide nanosheets. *Nat. Chem.* **5**, 263–275 (2013).
- Manzeli, S., Ovchinnikov, D., Pasquier, D., Yazyev, O. V. & Kis, A. 2D transition metal dichalcogenides. *Nat. Rev. Mater.* **2**, 17033 (2017).
- Avsar, A. et al. Colloquium: Spintronics in graphene and other two-dimensional materials. *Rev. Mod. Phys.* **92**, 021003 (2020).
- Ritter, K. A. & Lyding, J. W. The influence of edge structure on the electronic properties of graphene quantum dots and nanoribbons. *Nat. Mater.* **8**, 235–242 (2009).
- Magda, G. Z. et al. Room-temperature magnetic order on zigzag edges of narrow graphene nanoribbons. *Nature* **514**, 608–611 (2014).
- Cao, D., Shen, T., Liang, P., Chen, X. & Shu, H. Role of chemical potential in flake shape and edge properties of monolayer MoS<sub>2</sub>. *J. Phys. Chem. C* **119**, 4294–4301 (2015).
- Ren, Y. et al. Mo-edge reconstructions in MoSe<sub>2</sub> and MoS<sub>2</sub>: Reexamination of the mechanism. *Phys. Rev. B* **104**, 115406 (2021).
- Sang, X. et al. In situ edge engineering in two-dimensional transition metal dichalcogenides. *Nat. Commun.* **9**, 2051 (2018).
- Efetov, D. K. et al. Specular interband Andreev reflections at van der Waals interfaces between graphene and NbSe<sub>2</sub>. *Nat. Phys.* **12**, 328–331 (2016).
- Tang, S. et al. Quantum spin Hall state in monolayer 1T'-WTe<sub>2</sub>. *Nat. Phys.* **13**, 683–687 (2017).
- Kezilebieke, S. et al. Topological superconductivity in a van der Waals heterostructure. *Nature* **588**, 424–428 (2020).
- Lüpke, F. et al. Proximity-induced superconducting gap in the quantum spin Hall edge state of monolayer WTe<sub>2</sub>. *Nat. Phys.* **16**, 526–530 (2020).
- Stühler, R. et al. Tomonaga-Luttinger liquid in the edge channels of a quantum spin Hall insulator. *Nat. Phys.* **16**, 47–51 (2020).
- Xi, X. et al. Strongly enhanced charge-density-wave order in monolayer NbSe<sub>2</sub>. *Nat. Nanotechnol.* **10**, 765 (2015).
- Xi, X. et al. Ising pairing in superconducting NbSe<sub>2</sub> atomic layers. *Nat. Phys.* **12**, 139–143 (2016).
- Ugeda, M. M. et al. Characterization of collective ground states in single-layer NbSe<sub>2</sub>. *Nat. Phys.* **12**, 92–97 (2016).
- Dai, J. et al. Microscopic evidence for strong periodic lattice distortion in two-dimensional charge-density wave systems. *Phys. Rev. B* **89**, 165140 (2014).
- Gye, G., Oh, E. & Yeom, H. W. Topological landscape of competing charge density waves in 2H-NbSe<sub>2</sub>. *Phys. Rev. Lett.* **122**, 016403 (2019).
- Wilson, J. A., Di Salvo, F. J. & Mahajan, S. Charge-density waves and superlattices in the metallic layered transition metal dichalcogenides. *Adv. Phys.* **24**, 117–201 (1975).
- Nakata, Y. et al. Monolayer 1T-NbSe<sub>2</sub> as a Mott insulator. *NPG Asia Mater.* **8**, e321 (2016).
- Silva-Guillén, J. Á., Ordejón, P., Guinea, F. & Canadell, E. Electronic structure of 2H-NbSe<sub>2</sub> single-layers in the CDW state. *2D Mater.* **3**, 035028 (2016).
- Lian, C., Si, C. & Duan, W. Unveiling charge-density wave, superconductivity, and their competitive nature in two-dimensional NbSe<sub>2</sub>. *Nano Lett.* **18**, 2924–2929 (2018).
- Shao, G. et al. Shape-engineered synthesis of atomically thin 1T-SnS<sub>2</sub> catalyzed by potassium halides. *ACS Nano* **13**, 8265–8274 (2019).
- Giannozzi, P. et al. QUANTUM ESPRESSO: a modular and open-source software project for quantum simulations of materials. *J. Phys.: Condens. Matter* **21**, 395502 (2009).
- Perdew, J. P., Burke, K. & Ernzerhof, M. Generalized gradient approximation made simple. *Phys. Rev. Lett.* **77**, 3865–3868 (1996).
- Guster, B. et al. Coexistence of elastic modulations in the charge density wave state of 2H-NbSe<sub>2</sub>. *Nano Lett.* **19**, 3027–3032 (2019).
- Arguello, C. J. et al. Quasiparticle interference, quasiparticle interactions, and the origin of the charge density wave in 2H-NbSe<sub>2</sub>. *Phys. Rev. Lett.* **114**, 037001 (2015).
- Chen, M., Chen, X., Yang, H., Du, Z. & Wen, H. Superconductivity with twofold symmetry in Bi<sub>2</sub>Te<sub>3</sub>/FeTe<sub>0.55</sub>Se<sub>0.45</sub> heterostructures. *Sci. Adv.* **4**, eaat1084 (2018).
- Regel, J., Mashoff, T. & Elmers, H. J. Quasiparticle interference of spin momentum locked surface states at step edges on Re(0001). *Phys. Rev. B* **102**, 115404 (2020).
- Zhao, H. et al. Nematic transition and nanoscale suppression of superconductivity in Fe(Te,Se). *Nat. Phys.* **17**, 903–908 (2021).
- McMillan, W. L. Theory of discommensurations and the commensurate-incommensurate charge-density-wave phase transition. *Phys. Rev. B* **14**, 1496 (1976).
- Pásztor, Á. et al. Holographic imaging of the complex charge density wave order parameter. *Phys. Rev. Res.* **1**, 033114 (2019).
- Pásztor, Á. et al. Multiband charge density wave exposed in a transition metal dichalcogenide. *Nat. Commun.* **12**, 6037 (2021).

## Acknowledgements

This work is financially supported by National Natural Science Foundation of China (Nos. 61725107, 61971035, 61901038, 61922035, 11874171, 12074006), National Key Research and Development Program of China (Nos. 2019YFA0308000, 2020YFA0308800), Beijing Natural Science Foundation (Nos. Z190006, 4192054), and China Postdoctoral Science Foundation (2020M680382, 2021M700407). The computational resources are supported by the high-performance computing platform of Peking University.

## Author contributions

Y.Z., W.H.D., and Y.L.W. coordinated the research project. Q.Z.Z., T.Z., X.Y.H., Z.P.H., Y.Y.C., M.L., L.G.J., X.X.H., L.W.L., Y.Z., and Y.L.W. synthesized the samples and performed the STM experiments. J.H.F., J.Z.W., Y.M.X., and H.Q.H. performed the theoretical calculations. All authors analyzed the data and discussed the manuscript. Q.Z.Z., J.H.F., and T.Z. contributed equally to this work.

## Competing interests

The authors declare no competing interests.

**Additional information**

**Supplementary information** The online version contains supplementary material available at <https://doi.org/10.1038/s42005-022-00899-y>.

**Correspondence** and requests for materials should be addressed to Huaqing Huang, Yu Zhang or Yeliang Wang.

**Peer review information** *Communications Physics* thanks Yi Du, Pablo Ordejon, and the other, anonymous, reviewer(s) for their contribution to the peer review of this work.

**Reprints and permission information** is available at <http://www.nature.com/reprints>

**Publisher's note** Springer Nature remains neutral with regard to jurisdictional claims in published maps and institutional affiliations.



**Open Access** This article is licensed under a Creative Commons Attribution 4.0 International License, which permits use, sharing, adaptation, distribution and reproduction in any medium or format, as long as you give appropriate credit to the original author(s) and the source, provide a link to the Creative Commons license, and indicate if changes were made. The images or other third party material in this article are included in the article's Creative Commons license, unless indicated otherwise in a credit line to the material. If material is not included in the article's Creative Commons license and your intended use is not permitted by statutory regulation or exceeds the permitted use, you will need to obtain permission directly from the copyright holder. To view a copy of this license, visit <http://creativecommons.org/licenses/by/4.0/>.

© The Author(s) 2022